Scanning Electrochemical Microscopy as a Local Probe of Oxygen Permeability in Cartilage

Marylou Gonsalves,* Anna L. Barker,* Julie V. Macpherson,* Patrick R. Unwin,* Danny O'Hare,† and C. Peter Winlove‡

*Department of Chemistry, University of Warwick, Coventry CV4 7AL; †Department of Pharmacy, University of Brighton, Brighton BN2 4GJ; and ‡Physiological Flow Studies Group, Department of Biological and Medical Systems, Imperial College of Science Technology and Medicine, London SW7 2BY, United Kingdom

ABSTRACT The use of scanning electrochemical microscopy, a high-resolution chemical imaging technique, to probe the distribution and mobility of solutes in articular cartilage is described. In this application, a mobile ultramicroelectrode is positioned close (~1 μm) to the cartilage sample surface, which has been equilibrated in a bathing solution containing the solute of interest. The solute is electrolyzed at a diffusion-limited rate, and the current response measured as the ultramicroelectrode is scanned across the sample surface. The topography of the samples was determined using $Ru(CN)_6^{4-}$, a solute to which the cartilage matrix was impermeable. This revealed a number of pit-like depressions corresponding to the distribution of chondrocytes, which were also observed by atomic force and light microscopy. Subsequent imaging of the same area of the cartilage sample for the diffusion-limited reduction of oxygen indicated enhanced, but heterogeneous, permeability of oxygen across the cartilage surface. In particular, areas of high permeability were observed in the cellular and pericellular regions. This is the first time that inhomogeneities in the permeability of cartilage toward simple solutes, such as oxygen, have been observed on a micrometer scale.

INTRODUCTION

Permeability is a key factor governing transport rates in biological membranes and tissues (Fournier, 1999). Articular cartilage is a specialized biological tissue for which permeability and fluid transport have been particularly well-studied (Maroudas, 1975; Bernich et al., 1976; Allhands et al., 1984; Mow et al., 1984), due to the possible association between mass transport characteristics in the tissue and diseases such as rheumatoid and osteoarthritis (Keuttner et al., 1992; Muehleman and Arsenis, 1995).

Cartilage is a connective tissue which provides a smooth, shock-absorbing, cushioning surface at load-bearing diarthrodial joints. It is composed of an extracellular matrix (ECM) containing a gel of negatively charged proteoglycan molecules, cells (chondrocytes), and interstitial water, embedded in a porous supporting framework of collagen fibers (Shrive and Frank, 1994). Under normal physiological conditions, the water content constitutes ~70% of the tissue weight. The chondrocytes, though relatively sparse (<1% of the cartilage volume), are responsible for synthesizing, maintaining, and metabolizing the cartilage matrix components. Because cartilage is aneural and avascular, intercell communication and the transport of nutrients and waste products must be effected by diffusion through the matrix. Knowledge of the transport of solutes through the cartilage matrix is therefore crucial in understanding the physiological functioning of the tissue, both in the healthy and diseased states. In particular, it is thought that disturbances in fluid and solute transport through the cartilage matrix may contribute to, or result from, biochemical or structural changes in the tissue during the progression of osteoarthritis (Urban and Hall, 1992). However, traditional experimental methodologies have, as yet, been unable to probe mass transport with adequate spatial resolution to detect such changes either in vitro or in vivo.

A number of studies have been made on the bulk diffusion of solutes through cartilage (Maroudas, 1970; Bernich et al., 1976; Roberts et al., 1996; Torzilli et al., 1997, 1998). However, it is known that cartilage is structurally heterogeneous, evident from various microscopy studies (Horky, 1993; Jurvelin et al., 1996). Some workers have addressed this issue by taking samples (50–200 μm thick) at varying depths from the articular surface (Bernich et al., 1976; Torzilli et al., 1997, 1998), but data were still averaged *across the surface of the slice*, thereby neglecting any lateral inhomogeneities in transport rates. More recently, magnetic resonance imaging has emerged as a useful tool for the study of biological tissues, and a number of measurements of solute and water transport in cartilage have been reported (Burstein et al., 1993; Fischer et al., 1995; Knauss et al., 1996; Potter et al., 1997). This technique has the advantage of being non-invasive, with in vivo capabilities, and currently has the potential to achieve resolution on a scale of tens of micrometers (Potter et al., 1997). The technique is, however, limited to the study of paramagnetic species.

Scanning electrochemical microscopy (SECM) is a powerful technique for examining the diffusive, convective, and migratory transport of solutes. In SECM, an ultramicroelec-

Received for publication 10 June 1999 and in final form 14 December 1999.

Address reprint requests to Prof. P. R. Unwin, Department of Chemistry, University of Warwick, Coventry CV4 7AL, UK. Tel.: +44-24-7652-3264; Fax: +44-24-7652-4112; E-mail: P.R.Unwin@warwick.ac.uk.

0006-3495/00/03/1578/11 $2.00

trode (UME), attached to piezoelectric positioners, is mobile in three dimensions. The UME can be positioned close to an interface with submicron precision, and can probe the topography, reactivity, or permeability of that interface with high spatial resolution (Bard et al., 1991b; Barker et al., 1999). SECM has been applied to the study of a number of synthetic membranes and biomaterials including skin (Bath et al., 1998; Scott et al., 1991; 1993a, b; 1995), dentine (Macpherson et al., 1995a, b; Unwin et al., 1997), and bilayer lipid membranes (Matsue et al., 1994). SECM has the advantage over scanning ion conductance microscopy, which has found some application in the investigation of membrane transport (Hansma et al., 1989; Korchev et al., 1997), in that it can selectively detect both neutral and charged species, rather than measure total ion currents.

In a recent study we used SECM to image osmotically driven convective transport through laryngeal cartilage (Macpherson et al., 1997) and were able, for the first time, to correlate local convective fluxes with sample topography on a microscopic scale. The study of spatially resolved localized diffusion, however, has proved more difficult. To investigate the related transport properties of permeability and diffusion, we have recently introduced an SECM induced-transfer (SECMIT) approach (Barker et al., 1998). In SECMIT, a solute is partitioned between two phases at equilibrium. A UME, positioned in one phase close to the interface, is biased so as to deplete the local concentration of solute at the tip. This perturbs the equilibrium, driving the transfer of solute from the second phase to the tip. Hence, measurements of diffusion in the second phase can be made without the need to enter or contact the second phase, which is particularly advantageous for measurements in biological tissues where sample integrity is essential. However, this technique has not, as yet, been used to image variations in permeability across an interface.

In this paper we describe the use of SECMIT to probe the diffusive transport of solutes through cartilage in order to further understanding of the relationship between tissue structure and local permeability. Particular attention is given to oxygen, due to its general biological relevance and specific role in cartilage metabolism (Stockwell, 1983). The high-resolution capabilities of the technique offer the possibility of probing transport processes occurring at the level of a single cell. In future studies this will be particularly useful for monitoring the metabolic rates of chondrocytes. To examine viable (living) cartilage, a preliminary study is made here to investigate transport properties in non-metabolizing ECM tissue.

EXPERIMENTAL DETAILS

Materials

Bovine articular cartilage, from the metacarpal phalangeal joints of mature animals, was obtained fresh from the abattoir and stored at −20°C before use. Full-depth plugs of cartilage were removed from thawed joints using a 5 mm diameter cork borer and cut into 50-μm-thick sections parallel to the articular surface on a microtome (Model 5030, Bright Instruments, Huntington, UK).

Before SECM experiments, the sections were equilibrated in a 0.2 mol dm^{-3} potassium chloride (analytical reagent, Fisons, UK) solution, phosphate-buffered to pH 7.0 ± 0.2. SECM approach curves, imaging measurements, and atomic force microscopy (AFM) were carried out with the cartilage sample bathed in a solution containing 5×10^{-3} mol dm^{-3} potassium hexacyanoruthenate (II) ($K_4Ru(CN)_6$) (Alfa, Royston, UK) and 0.2 mol dm^{-3} potassium chloride, phosphate-buffered to pH 7.0 ± 0.2. Chronoamperometric measurements were made in 0.02 mol dm^{-3} $K_4Ru(CN)_6$ and 0.2 mol dm^{-3} potassium chloride, phosphate-buffered to pH 7.0 ± 0.2. Samples were allowed to soak in the bathing solution for at least 1 h before measurements. Given the thinness of the samples, this was sufficient time for the system to equilibrate. All solutions were prepared under ambient conditions, and measurements were made at room temperature (22 ± 2°C). Representative cartilage sections were stained for histological analysis using standard protocols (Carleton, 1980): van Gieson's stain for collagen, hematoxylin, and eosin for cell nuclei and toluidine blue for proteoglycans.

Instrumentation

The general SECM set-up has been described previously (Macpherson et al., 1995a). For tip approach experiments, the UME was a 25-μm-diameter platinum disk electrode, embedded in a glass insulating sheath with the overall tip diameter 10 times that of the Pt disk, i.e., 250 μm. A 5-μm-diameter platinum disk electrode, embedded in a glass capillary, with an overall tip diameter of 50 μm, was used for all imaging and chronoamperometric measurements. The UME served as the working electrode in a conventional two-electrode set-up, with a silver wire quasi-reference electrode (AgQRE), against which all potentials are quoted. For chronoamperometric measurements, the current-time transients were recorded on a digital oscilloscope (Model NIC-310, Nicolet Technologies, Milton Keynes, UK).

The 50-μm-thick cartilage sections were fixed on a glass disk (diameter 12.7 mm, thickness 1.6 mm) using a 1:1 volume mixture of nail varnish and cyanoacrylate glue applied around the circumference of the sample, while ensuring that the sample remained flat and hydrated during the fixing procedure. The glass disk was then mounted in the base of an SECM cell so that the disk was perpendicular to the UME tip axis. Optical micrographs of the samples were taken using an Olympus BH2 microscope equipped with a 3-CCD color video camera (model KY-F55BE, JVC Professional, London, UK) coupled to a computerized data acquisition system (Image Grabber/PCI, Neotech Ltd., London, UK).

AFM images were made in contact mode under solution using a Nanoscope E atomic force microscope and fluid cell (Digital Instruments, Santa Barbara, CA). The silicon nitride AFM probe had a nominal spring constant of 0.06 N m^{-1}.

Procedures

Tip approach measurements

Tip approach curves were acquired by holding the UME, of radius a = 12.5 μm, at a fixed x-y location (Fig. 1 *A*), and the current response for the diffusion-limited electrolysis of the solute measured as the UME was translated in the z-direction from a position in bulk solution to one close to the interface. The tip potential was held at a value where electrolysis of the solute was diffusion-limited, identified by recording a steady-state voltammogram. This was 1.2 V for $Ru(CN)_6^{4-}$ oxidation and −0.5 V for O_2 reduction. The UME was then scanned toward the interface at a velocity of 1 μm s^{-1}, and the limiting current response, i (normalized with respect to

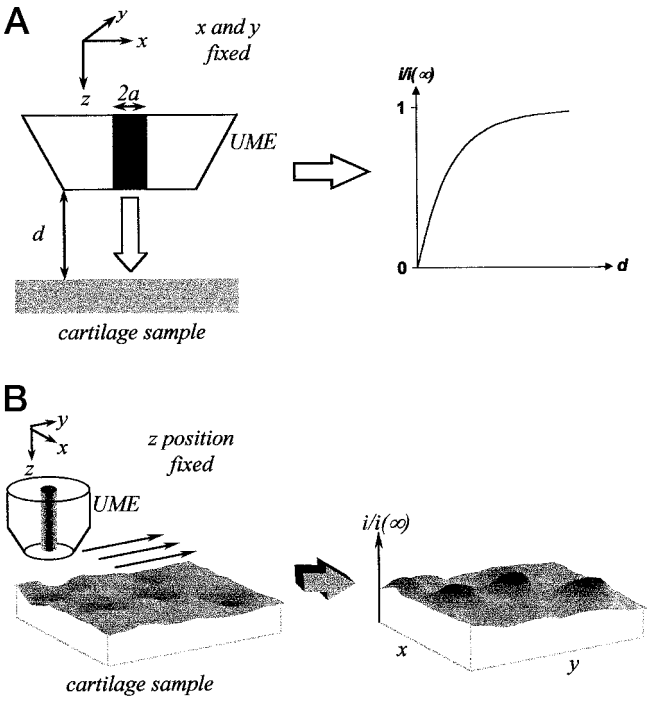

FIGURE 1 Schematics depicting the different modes of SECM operation for (*A*) tip approach measurements and (*B*) imaging experiments (not to scale).

the steady-state current with the tip positioned at an effectively infinite distance from the sample interface, $i(\infty)$), recorded as a function of tip-sample separation, d. By analyzing the $i/i(\infty)$-d curves, the transport properties of the solutes of interest in cartilage were analyzed using a theory outlined in full elsewhere (Barker et al., 1998).

SECM imaging

SECM images were obtained by holding the UME tip ($a = 2.5\ \mu$m) at a constant z position and scanning in the x-y plane over an area of interest (Fig. 1 *B*). For a solute to which the cartilage was impermeable, changes in the diffusion-limited current response were due to variations in the sample-tip separation, from which topographical information on the sample surface could be obtained (Mirkin et al., 1992). When the same sample area was subsequently scanned, using a solute toward which cartilage was permeable, the current response provided a permeability map of the area.

For $Ru(CN)_6^{4-}$ oxidation the tip was held at a potential of 1.2 V. After recording the steady-state current, $i(\infty)$, with the tip positioned far from the surface, the height of the UME tip above the cartilage sample was adjusted until $i/i(\infty)$ attained a value of 0.25. Based on the data herein, this corresponded to a sample-tip separation of $\sim 1\ \mu$m. The UME was then scanned over a 100 μm $\times$ 100 μm area at 5 μm s^{-1} in unidirectional lines with a separation of 5 μm between line scans, and the tip current recorded as a function of lateral tip position. At the end of the scan, the UME was retracted 200 μm from the cartilage surface and the bulk solution limiting current verified.

For oxygen permeability scans the UME was moved to the same initial position as for the $Ru(CN)_6^{4-}$ oxidation scans, and repolarized to -0.5 V for diffusion-limited oxygen reduction. The UME was scanned over the same 100 μm $\times$ 100 μm area at the same scan rate.

Chronoamperometry

For chronoamperometry, the UME was positioned over an area of interest (identified from SECM imaging), close to the tissue/bathing solution interface, and the current recorded as a function of time after jumping the potential from a value where no current flowed to one where solute electrolysis was diffusion-limited. All chronoamperometric measurements were made at a 5 μm diameter Pt UME with $Ru(CN)_6^{4-}$ as the solute.

RESULTS AND DISCUSSION

The results presented herein are for a single cartilage sample, but are typical of >20 samples studied.

Structural and chemical characterization of the cartilage surfaces

Cartilage is known to be structurally and chemically heterogeneous on a local (submicron) scale (Shrive and Frank, 1994). Fig. 2 shows a light micrograph of an area of cartilage comparable to that scanned by the SECM. A number of pit-like features can be clearly observed, with diameters ranging from 15 μm to 25 μm. An AFM image of a neighboring field, recorded under solution, is shown in Fig. 3. Again, a number of recessed regions are clearly visible, with diameters of $\sim$20 μm and depths of 2–3 μm. These recesses correspond to cells or, more usually, groups of two or more cells. Although the pericellular matrix may have been distorted during the freezing/thawing process, the nucleus is still intact in the majority of cells. In the interterritorial matrix, surface irregularities are of the order of a micron in depth.

The rate of water and solute transport through the cartilage matrix is expected to be greatly influenced by the local biochemical composition, based on observations for other tissues (Weinberg et al., 1997). Micrographs of histologically stained cartilage sections are shown in Fig. 4. On this scale, the nuclei and cell boundaries are clearly visible.

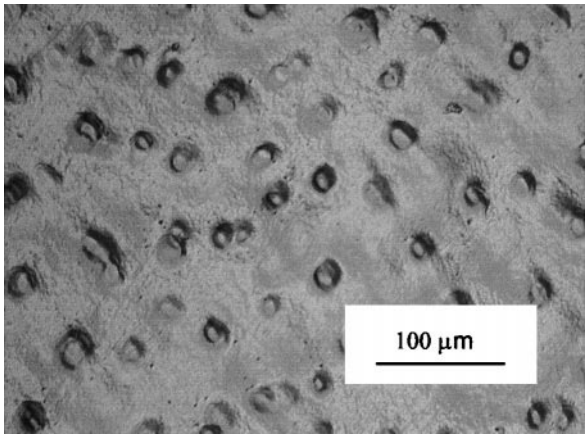

FIGURE 2 Light micrograph of a cartilage section.

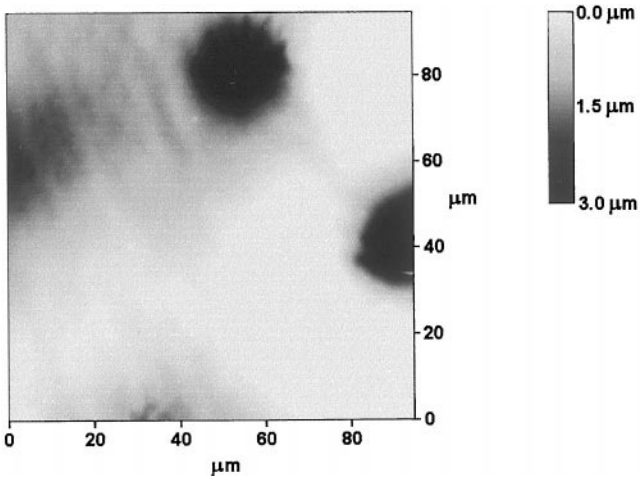

FIGURE 3 Atomic force microscopy image of a cartilage section, recorded under solution (5×10^{-3} mol dm^{-3} $K_4Ru(CN)_6$ and 0.2 mol dm^{-3} KCl, phosphate-buffered to pH 7 $\pm$ 0.2).

Collagen staining is light in the cellular and pericellular regions, and most intense in the interterritorial region, some distance from the cells. In the case of proteoglycan, the staining is lightest in the area surrounding the nucleus and more intense in the pericellular and interterritorial regions. This pattern of staining is similar to that observed in previous studies (Hunziker et al., 1997).

Tip approach measurements

In order to determine the surface topography of the cartilage sample under SECM conditions, a solute was required that did not permeate the matrix. An initial estimate of the permeability of solutes in the cartilage matrix was obtained by analyzing the $i/i(\infty)$ response of the UME tip as it approached the interface. By using a relatively large UME, the tip response is averaged over a sizeable area and approaches that representative of the "bulk" behavior of the cartilage. As the topographical features on the cartilage surface are on the order of a few microns in depth, the surface may be considered as approximately planar (for the approach by a large UME).

$Ru(CN)_6^{4-}$ oxidation

$Ru(CN)_6^{4-}$ is a large, highly charged anion, and so would not be expected to significantly permeate the matrix, as cartilage is negatively charged at physiological pH (Maroudas, 1975). Typical approach curves for $Ru(CN)_6^{4-}$ oxidation at a 25 μm diameter UME approaching both a flat glass disk and cartilage tissue are shown in Fig. 5. The experimental responses are seen to be in excellent agreement with the theoretical prediction for an impermeable planar substrate (Kwak and Bard, 1989) in both cases. The tip is able to attain a slightly closer distance to the glass surface than the cartilage surface due to the irregularities in the topography of the latter structure. Nevertheless, the tip is able to approach the cartilage surface to within a micron, and the data clearly demonstrate that $Ru(CN)_6^{4-}$ shows negligible induced-diffusion through the cartilage, making it a suitable solute for topographical measurements.

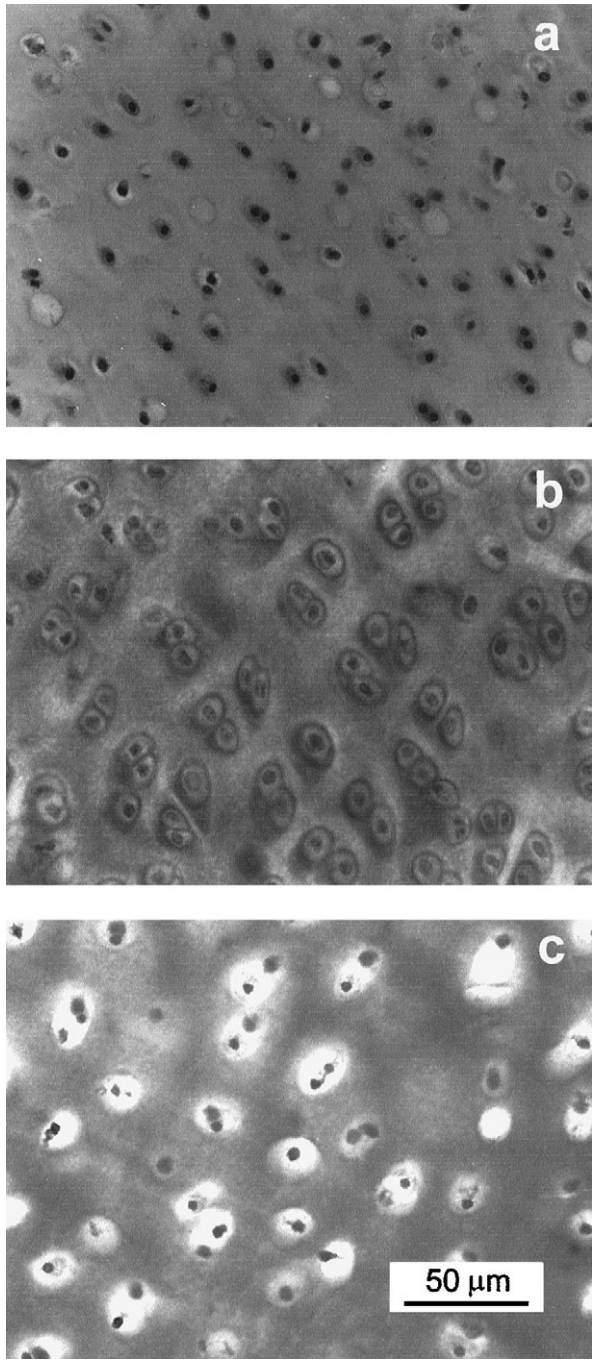

FIGURE 4 Light micrographs of histologically stained cartilage sections: (*a*) hematoxylin and eosin for cell nuclei, (*b*) toluidine blue for proteoglycans, and (*c*) van Gieson's stain for collagen.

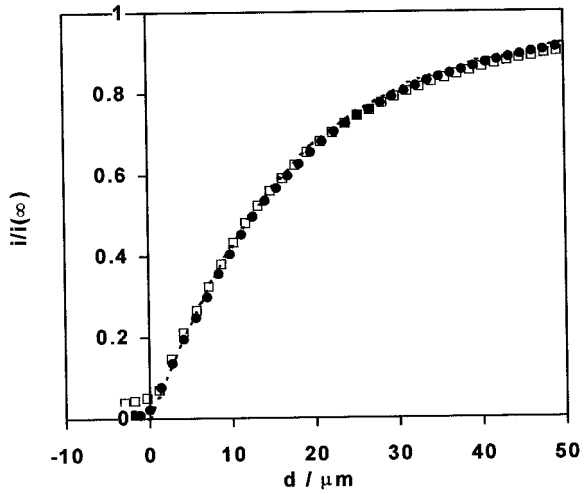

FIGURE 5 Approach curves of normalized current versus sample-tip separation for the diffusion-controlled oxidation of $Ru(CN)_6^{4-}$ at a 25 μm diameter Pt UME approaching cartilage (□) and a flat glass surface (●). The dashed line represents the theoretical response for approach to an impermeable substrate (Kwak and Bard, 1989).

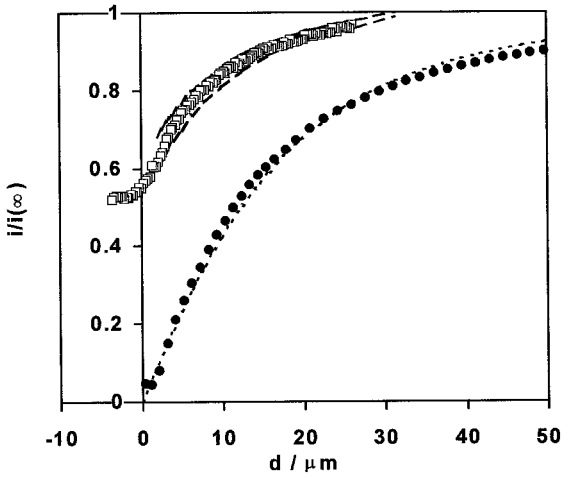

FIGURE 7 Approach curve of normalized current versus sample-tip separation for the diffusion-controlled reduction of oxygen at a 25-μm-diameter Pt UME approaching cartilage (□) and a flat glass surface (●). The short-dashed line represents the theoretical response for approach to an impermeable substrate (Kwak and Bard, 1989). The long-dashed lines represent the theoretical response for induced diffusion for different values of $K_e\gamma$ (Barker et al., 1998): 0.6 (*top line*) and 0.5 (*bottom line*).

Oxygen reduction

Oxygen is a small, neutral molecule that permeates tissues and membranes (Bicher and Bruley, 1973). Fig. 6 is a typical voltammogram for the reduction of oxygen at a 25-μm-diameter tip, clearly showing that the electrolysis process is diffusion-limited at a potential of -0.5 V, used for the approach curve measurements shown in Fig. 7. The experimental response in Fig. 7 for the cartilage surface does not fit the theory for approach to an impermeable substrate, found when the same experiment is carried out at a flat glass surface, the data for which are also shown in Fig. 7. Rather, the current is significantly higher than the theoretical response *at all values of d*. There is still a significant current ($i/i(\infty) \sim 0.5$) at the point where the UME contacts the cartilage surface. We therefore deduce that the UME promotes diffusion of O_2 through the cartilage matrix to the tip: local depletion of O_2 in the tip-substrate gap induces transfer from the sample to solution to restore equilibrium. Hence, the approach curves demonstrates that oxygen shows appreciable permeability in cartilage.

The relative permeability of a solute in cartilage, compared to the bathing solution, may be expressed as the product, $K_e\gamma$ (Maroudas, 1975), where K_e is the partition coefficient of the solute in the cartilage (ratio of the concentration in the cartilage to that in the contacting solution) and γ is the ratio of the solute diffusion coefficient in cartilage to that in solution. Theoretical simulations (Barker et al., 1998) of $i/i(\infty)$ vs. d at different $K_e\gamma$ values indicate that a value of $K_e\gamma$ between 0.5 and 0.6 best describes the experimental data, as indicated by the dashed lines in Fig. 7. This is similar to the value of $K_e\gamma$ measured previously for oxygen in laryngeal cartilage (Macpherson et al., 1997).

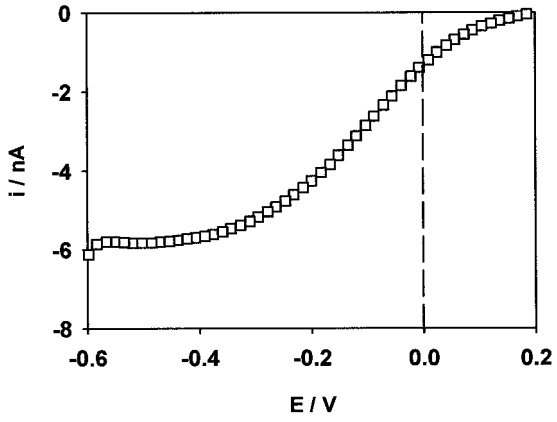

FIGURE 6 Linear sweep voltammogram for the reduction of oxygen at a 25-μm-diameter Pt UME in a solution containing 5×10^{-3} mol dm^{-3} ($K_4Ru(CN)_6$) and 0.2 mol dm^{-3} potassium chloride, phosphate-buffered to pH 7.0 $\pm$ 0.2, recorded at a scan rate of 20 mV s^{-1}.

SECM imaging

Sample topography

For the reasons outlined above, $Ru(CN)_6^{4-}$ was used to image the cartilage topography. A typical contour plot of normalized current as a function of lateral probe position for $Ru(CN)_6^{4-}$ oxidation is shown in Fig. 8. The dark areas indicate higher $i/i(\infty)$ values. Clearly, the $i/i(\infty)$ response is heterogeneous over the scanned area. There are well-defined circular regions of enhanced current. Under steady-state conditions the sample-tip separation, d, can be evalu-

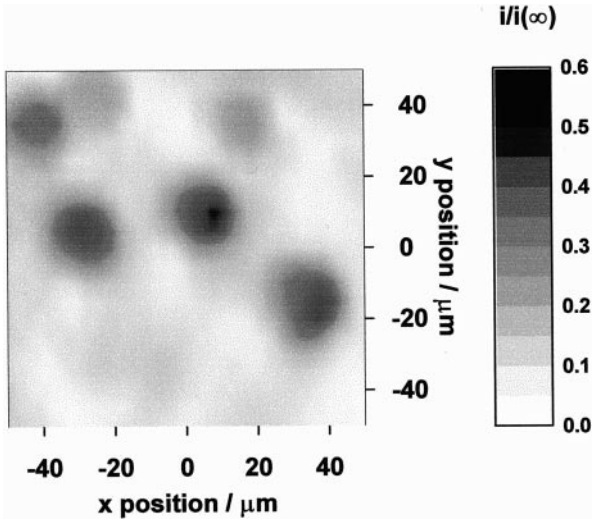

FIGURE 8 Contour plot showing the normalized current map for a 100 × 100 μm area of cartilage, imaged using the diffusion-controlled oxidation of $Ru(CN)_6^{4-}$ at a 5-μm-diameter Pt UME at an initial sample-tip separation of ~2 μm.

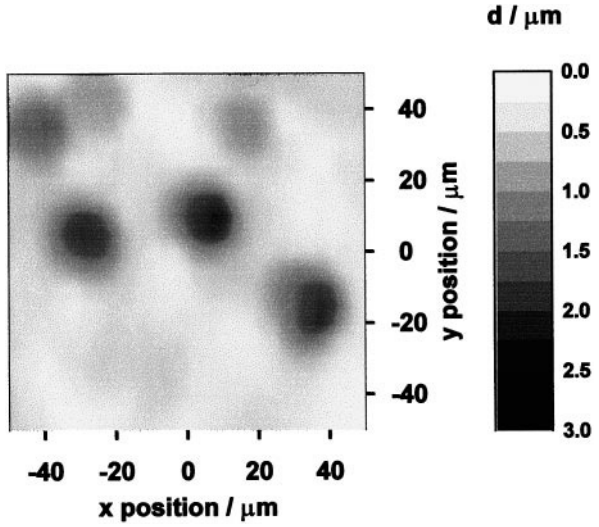

FIGURE 9 Contour plot showing the corresponding topography map, calculated from Eq. 1, for the area of cartilage imaged in Fig. 8.

ated from the following relationship between $i/i(\infty)$ and d (Mirkin et al., 1992):

$$\frac{i}{i(\infty)} = \left[0.292 + \frac{1.515}{d/a} + 0.655 \exp\left(-\frac{2.403}{d/a}\right)\right]^{-1} \quad (1)$$

Although this equation strictly applies to a planar interface, it provides useful semi-quantitative information on sample topography (Bard et al., 1994). For the electrode used in this study the residence time in the vicinity of a spot on the sample, t_{res}, is 1 s (where $t_{res} = 2a/v_{tip}$, and v_{tip} is the tip scan speed). This is more than sufficient time for steady-state conditions to be established (Bard et al., 1991a).

Fig. 9 shows the topography image derived, using Eq. 1, from the normalized current data in Fig. 8. It can be seen that the circular regions of current in Fig. 8 correspond to pits in the cartilage surface of diameter 15 to 25 μm and depths between 2 and 3 μm. These dimensions are in excellent agreement with the topographical features observed by optical microscopy and AFM (Figs. 2 and 3), demonstrating that for this particular surface, hindered diffusion imaging provides a good means of determining sample topography.

For the permeability studies that follow, it was essential that the $Ru(CN)_6^{4-}$ data gave a true representation of the sample topography. As an additional check on the impermeability of cartilage to $Ru(CN)_6^{4-}$, and as a complement to the approach curve measurements made with the large electrode, high-resolution chronoamperometric measurements were made at defined positions close to the interface. In particular, we were interested in further demonstrating that the electrochemical imaging method provided an accurate picture of the topography of the recessed regions. Chronoamperometry has been shown to be particularly sensitive to the partition coefficient and relative diffusion coefficients of solutes in two-phase systems (Barker et al., 1998). For these studies, an area of cartilage was initially imaged with $Ru(CN)_6^{4-}$ to identify a single pit, followed by chronoamperometric measurements at a fixed point in the recess. Fig. 10 shows typical results, made at $d = 0.6$ μm, presented as $i/i(\infty)$ vs. t (A) and $t^{-1/2}$ (B) so as to emphasize the long and short time behavior, respectively, for $Ru(CN)_6^{4-}$ oxidation close to the cartilage surface. Also shown is the theoretical response at an impermeable substrate for a $\log(d/a)$ value of -0.6. The observation of close agreement between theory and experiment over a wide time scale further confirms that, under the conditions of our SECM experiments, $Ru(CN)_6^{4-}$ can be considered as having negligible permeability in the cartilage matrix.

Oxygen permeability

Fig. 11 shows a diffusion-limited current map for oxygen reduction recorded with the tip in the same z position and over the same area considered for Figs. 8 and 9. Similar circular regions of enhanced current can be seen, as were found in Fig. 8. However, the overall $i/i(\infty)$ values are higher than those observed for the $Ru(CN)_6^{4-}$ oxidation image (Fig. 8), which can be attributed to the induced diffusion of oxygen through the cartilage matrix. Using a computer simulation (Barker et al., 1998), the effect of permeability, defined as $K_e\gamma$, on $i/i(\infty)$ was evaluated as a function of sample-tip separation, from which the relationship between $i/i(\infty)$, d, and $K_e\gamma$ was derived. In this way, the normalized current data for O_2 reduction was processed to take account of the varying tip-substrate separation (Fig. 9), yielding a map of oxygen permeability in the cartilage

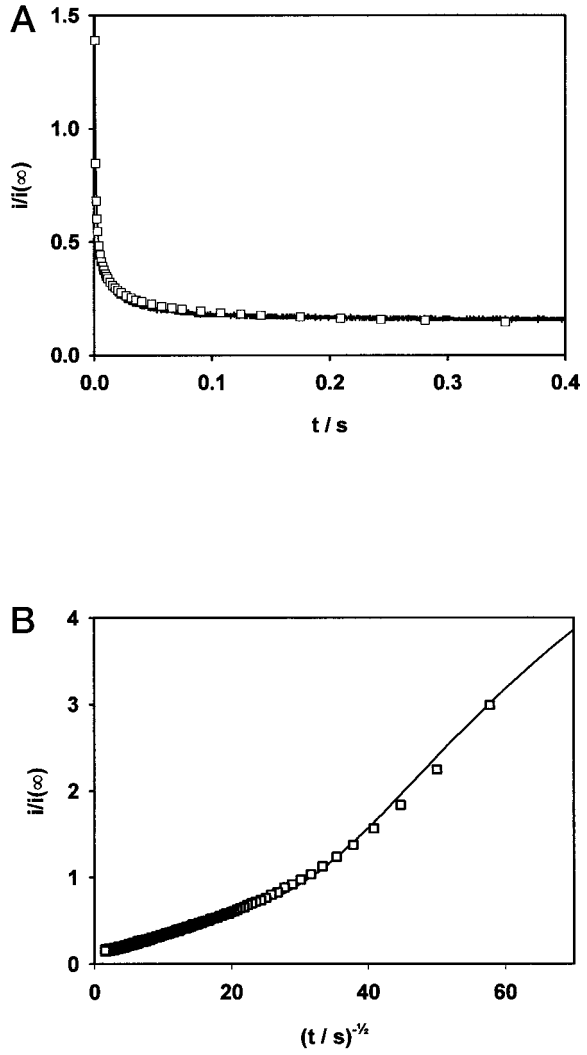

FIGURE 10 Plots of $i/i(\infty)$ vs. (*A*) t and (*B*) $t^{-1/2}$ for the diffusion-controlled oxidation of $Ru(CN)_6^{4-}$ at a 5-μm-diameter Pt UME recorded at $d = 0.6$ μm from the cartilage surface (□). The theoretical response for an impermeable substrate with the tip at a $\log(d/a)$ of -0.6 is also shown (———).

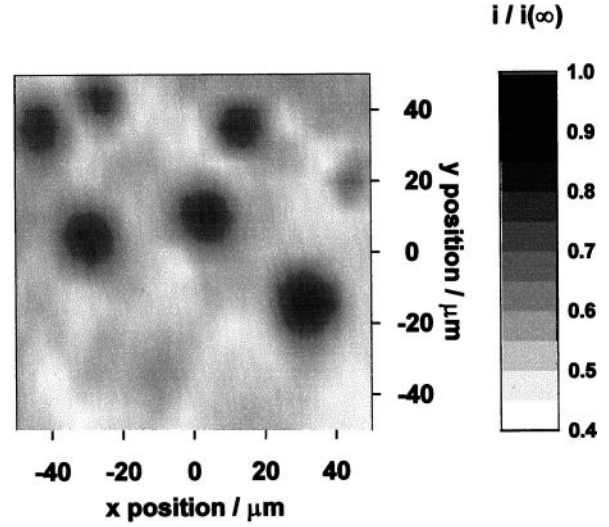

FIGURE 11 Contour plot showing the normalized current map for the diffusion-controlled reduction of oxygen at a 5-μm-diameter Pt UME, in the area of cartilage considered in Fig. 8.

sample. A permeability plot for the $i/i(\infty)$ data in Fig. 11 is shown in Fig. 12. It is evident that the permeability is not uniform. Significant variations are observed: the value of $K_e\gamma$ ranges from ~0.4 over most of the interterritorial matrix to 0.7 over the recesses in the cartilage surface, corresponding to the cells. Considering the data in Fig. 12 together with the histochemical composition of cartilage (Fig. 4), it is evident that there is high oxygen permeability in the cellular and pericellular regions. The intensity of toluidine blue staining, seen in Fig. 4 *b*, indicates a higher fixed charge density in the pericellular matrix. Whether this arises from differences in the type, organization, or accessibility of the proteoglycans is unclear. However, the higher staining intensity does not correspond to an increase in oxygen permeability, favoring the latter possibility. Evidence from various sources indicates that glycosaminoglycans have only a small effect on the diffusivity of small solutes (Gribbon et al., 1998). There is a strong relationship, however, between permeability and the intensity of collagen staining by van Gieson's stain (Fig. 4 *c*), with the lowest permeability observed in regions of intense staining. Although factors such as collagen type and fiber organization, as well as collagen content, influence the staining intensity, it is probable that collagen content affects the diffusivity and/or distribution of the analytes, both of which contribute to the measured permeability. This is the first time that lateral heterogeneities of solute permeability in cartilage have been observed on a micrometer scale.

The analysis of the oxygen permeability data assumes a planar interface. In order to ascertain that the large enhance-

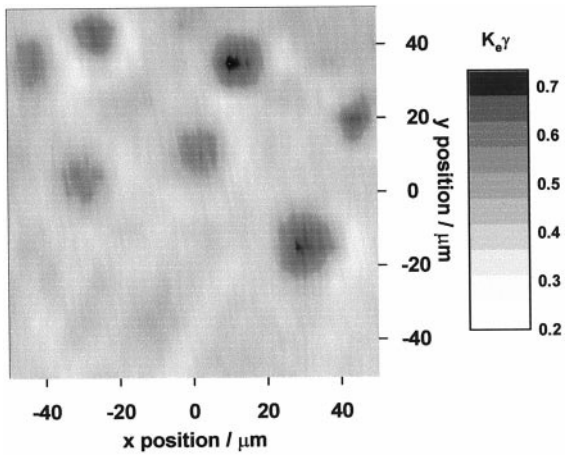

FIGURE 12 Oxygen permeability ($K_e\gamma$) map calculated from the normalized currents in Fig. 11.

ments in oxygen reduction currents observed over the recessed regions were not simply due to the non-planar geometry of the interface in these locations, a new SECM model was developed to predict the steady-state response with a UME close to and directly over a symmetrical recess. The simulations and theoretical results, summarized in the Appendix, showed that for the $K_e\gamma$ values of interest, a planar substrate model suffices to a good approximation for the situation where the tip is directly above a depression in the surface. While there may be higher-order effects from the heterogeneous nature of the substrate topography, the results in Fig. 12 represent a good description of the variation in oxygen permeability in the surface region of cartilage.

CONCLUSIONS

This study has shown SECMIT to be a powerful tool for probing diffusion processes in cartilage tissue, specifically allowing oxygen diffusion through the cartilage matrix to be correlated with tissue morphology. Enhanced oxygen diffusion has been detected in areas that are low in collagen content. This is the first time that lateral inhomogeneities in tissue permeability have been observed on a micrometer-length scale.

Following this preliminary study on non-metabolizing cartilage tissue, we should now be able to examine metabolic processes occurring in viable cartilage tissue. As previously demonstrated (Macpherson et al., 1997), SECM measurements of transport can be made in cartilage both in the presence and absence of an applied pressure. Hence, measurements should be possible under conditions similar to those of in vivo loaded cartilage, which is particularly important for the metabolic studies. We also plan to examine transport processes in both healthy and diseased cartilage. Finally, it should be noted that the measurement of spatially resolved diffusion processes using the SECM protocol described in this paper has considerable potential application to a wide range of biological tissues and membranes.

APPENDIX

Effect of substrate geometry on the SECM tip current response

The SECM induced-transfer (SECMIT) technique can be used to probe the permeability of a target solute in a sample not in direct contact with the UME. Details of the numerical model developed for this approach with a planar surface have been given previously (Barker et al., 1998). The following brief account outlines the formulation of a numerical model applicable to substrates with more complex geometry; in particular, for surfaces that contain pit-like depressions, which more closely resemble the biological samples studied in this paper.

The principle of the SECMIT methodology and the coordinate system used to define the new model are illustrated in Fig. 13. The UME is positioned in the aqueous phase (phase 1) close to the surface of the substrate (phase 2), directly above a circularly symmetric pit in the surface,

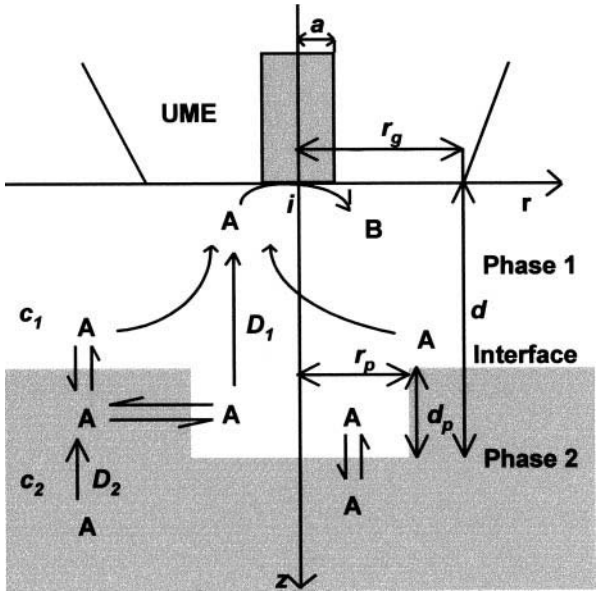

FIGURE 13 The coordinate system used to define the model outlined in the Appendix. The coordinates r and z are in the directions radial and normal to the electrode surface, respectively. The electrode radius is denoted by a, r_g is the distance from the center of the electrode to the outermost edge of the insulating glass sheath surrounding the electrode, r_p is the radius of the circularly symmetric pit in the surface of the substrate (phase 2), d is the distance from the surface of the electrode to the bottom of the pit, and d_p is the height of the pit. Phase 2 is considered to extend a semi-infinite distance in the z-direction. Species A is the common electroactive mediator in the two phases, while B denotes the product of the electrode reaction.

such that the combined tip/substrate geometry is axisymmetric. The two phases contain a common electroactive species, A. The interface between the two phases is assumed to be sharply defined and the transfer of species A across the interface is not kinetically limited. Initially, with the partitioning of A across the interface in dynamic equilibrium, there is zero net flux of species A across the interface and each phase has a uniform bulk concentration of A, c_i^*, where $i = 1$ or 2 denotes the phase. A potential step is subsequently applied to the UME sufficient to electrolyze species A at a diffusion-controlled rate. This perturbs the interfacial equilibrium, inducing transfer of species A across the interface from phase 2 to phase 1. The flux of species A to the UME, and hence the tip-current response, are dependent on the rate of mass transfer of the species in each phase.

Formulation of the problem

Time-dependent diffusion equations, appropriate to the axisymmetric SECM geometry, can be written for the species A in each phase.

$$\frac{\partial c_i}{\partial t} = D_i\left[\frac{\partial^2 c_i}{\partial r^2} + \frac{1}{r}\frac{\partial c_i}{\partial r} + \frac{\partial^2 c_i}{\partial z^2}\right] \times \begin{pmatrix} i = 1 & \text{for} & 0 \le r \le r_g; & 0 < z < d - d_p \\ & & 0 \le r \le r_p; & d - d_p < z < d \\ i = 2 & \text{for} & r_p < r \le r_g; & d - d_p < z < d \\ & & 0 \le r \le r_g; & z > d \end{pmatrix} \quad \text{(A1)}$$

where r and z are the coordinates in the directions radial and normal to the electrode surface, respectively, measured from the center of the electrode;

c_i and D_i are the concentration and diffusion coefficient of the electroactive species, A, in phase i; and t is time. As shown in Fig. 13, r_g denotes the radius of the probe (electrode plus insulating sheath), r_p is the radius of the pit, d represents the separation between the end of the probe and the bottom of the pit, and d_p is the depth of the pit. The calculation of the tip current response involves solving the diffusion equation A1, subject to the boundary and initial conditions of the system. Before the potential step, the initial condition is

$t = 0$:

$$c_i = c_i^* \begin{pmatrix} i = 1 & \text{for} & 0 \le r \le r_g; & 0 < z < d - d_p \\ & & 0 \le r \le r_p; & d - d_p < z < d_p \\ i = 2 & \text{for} & r_p < r \le r_g; & d - d_p < z < d \\ & & 0 \le r \le r_g; & z > d \end{pmatrix} \tag{A2}$$

Following the potential step, A is electrolyzed at a diffusion-controlled rate at the electrode, but is inert with respect to the insulating glass sheath surrounding the electrode, and remains at bulk concentration values beyond the radial edge of the tip. The exterior boundary conditions may be summarized as follows:

$$z = 0, \quad 0 \le r \le a: \qquad c_1 = 0 \tag{A3}$$

$$z = 0, \quad a < r \le r_g: \qquad D_1 \frac{\partial c_1}{\partial z} = 0 \tag{A4}$$

$$r > r_g, \qquad c_i = c_i^* \begin{pmatrix} i = 1 & \text{for} & 0 < z < d - d_p; \\ i = 2 & \text{for} & z > d - d_p \end{pmatrix} \tag{A5}$$

This latter condition is valid provided that $RG = r_g/a \ge 10$, where a is the radius of the electrode (Kwak and Bard, 1989).

The axisymmetric SECM geometry implies there is no radial flux of species A at the cylindrical axis of symmetry:

$$r = 0, \quad D_i \frac{\partial c_i}{\partial r} = 0 \quad \begin{pmatrix} i = 1 & \text{for} & 0 < z < d; \\ i = 2 & \text{for} & z > d \end{pmatrix} \tag{A6}$$

At a semi-infinite distance from the electrode, in phase 2, the electroactive species attains its bulk concentration, c_2^*.

$$z \to \infty, \qquad 0 \le r \le r_g: \qquad c_2 = c_2^* \tag{A7}$$

The final internal boundary conditions apply to the surface of the substrate:

$$c_{2,\text{int}} = K_e c_{1,\text{int}} \tag{A8}$$

$$D_{1,\text{int}}\left(\frac{\partial c_{1,\text{int}}}{\partial z}\right) = D_{2,\text{int}}\left(\frac{\partial c_{2,\text{int}}}{\partial z}\right) \tag{A9}$$

for

$$z = d - d_p, \quad r_p < r < r_g; \qquad z = d, \quad r < r_p;$$

$$d - d_p < z < d, \quad r = r_p$$

where $c_{i,\text{int}}$ is the concentration of A at the interface in phase i and $K_e = c_2^*/c_1^*$.

To formulate a general solution, the diffusion equations and boundary conditions were cast into dimensionless form through the introduction of the following normalized terms:

$$\tau = \frac{tD_1}{a^2} \tag{A10}$$

$$R = \frac{r}{a} \tag{A11}$$

$$Z = \frac{z}{a} \tag{A12}$$

$$\gamma = \frac{D_2}{D_1} \tag{A13}$$

$$C_i = \frac{c_i}{c_i^*} \qquad \text{where } i \text{ denotes either 1 or 2.} \tag{A14}$$

The aim of the calculation was to determine the tip current response as a function of time and tip/interface separation for particular $K_e\gamma$ values. The UME current is related to the flux of c_1 at the electrode surface,

$$i = 2\pi n a D_1 c_1^* \int_0^1 \left(\frac{\partial C_1}{\partial Z}\right)_{Z=0} R\, dR \tag{A15}$$

where n is the number of electrons transferred per redox event and F is Faraday's constant.

The normalized current ratio is given by:

$$\frac{i}{i(\infty)} = \frac{\pi}{2} \int_0^1 \left(\frac{\partial C_1}{\partial Z}\right)_{Z=0} R\, dR \tag{A16}$$

where $i(\infty)$ is the steady-state diffusion-limited current at an inlaid disk electrode positioned at an effectively infinite distance from the interface

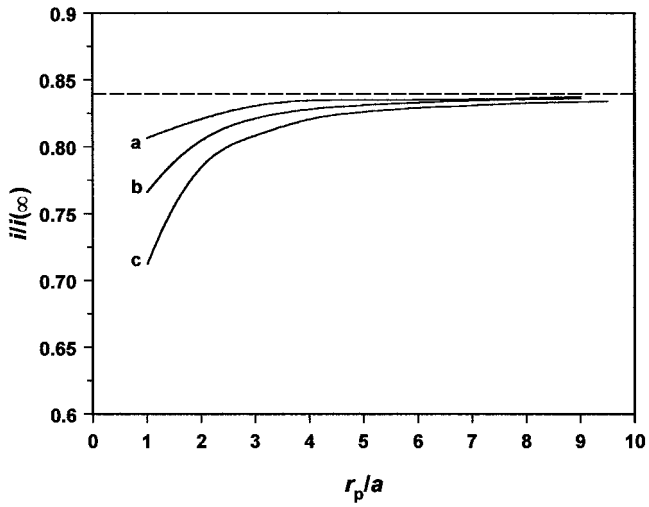

FIGURE 14 Simulated normalized steady-state current as a function of normalized pit radius (r_p/a) for $\gamma = 0.5$, $K_e = 1$, and a distance $d/a = 0.8$. Normalized pit depths, d_p/a, take the values (*a*) 0.2, (*b*) 0.4, (*c*) 0.6. The dashed line represents the steady-state current predicted for a UME at a distance $d/a = 0.8$ above a planar surface.

(Saito, 1968),

$$i(\infty) = 4nFaD_1c_1^* \quad \text{(A17)}$$

The problem was solved numerically using the alternating direction implicit finite-difference method (ADIFDM). General details on the application of this method to solve a variety of SECM problems have been given previously (see, for example, Barker et al., 1998). The modifications required to treat the present problem are straightforward and will not be discussed further. The ADIFDM method evaluates the current-time response of the UME; however, for the present problem only the steady-state current, derived from the chronoamperometric data in the long time limit, was of interest.

Simulations were performed for parameter values appropriate to the experimental system under study, using $\gamma = 0.5$ and $K_e = 1$ and a UME characterized by $RG = 10$. The plot in Fig. 14 shows the steady-state current as a function of normalized pit radius (r_p/a) for a fixed value of $d/a = 0.8$ (which for a UME with a radius of 2.5 μm corresponds to $d = 2$ μm) for three different pit wall depths. For a large pit radius, i.e., $r_p/a \rightarrow 10$, the steady-state current for all pit depths approaches that predicted for a planar substrate at a distance of $d/a = 0.8$ from the electrode, plotted as the dashed line in Fig. 14. As the radius of the pit is decreased the steady-state current decreases below this limit. The effect is particularly pronounced as the pit depth, d_p is increased. For the recesses observed in the cartilage surface in this study, r_p/a can approach 5, and it is clear that under these conditions the assumption of a planar interface in deriving permeability data is a good approximation for the typical tip-substrate separations employed.

The authors thank Rosemary Ewins for preparation and histological staining of the samples.

M.G. gratefully acknowledges financial support from the Wellcome Trust. A.L.B. and J.V.M thank the EPSRC for support.

REFERENCES

Allhands, R. V., P. A. Torzilli, and F. A. Kallfelz. 1984. Measurement of diffusion of uncharged molecules in articular cartilage. *Cornell Vet.* 74:111–123.

Bard, A. J., G. Denuault, R. A. Freisner, B. C. Dornblaser, and L. Tuckerman. 1991a. Scanning electrochemical microscopy: theory and application of the transient (chronoamperometric) SECM response. *Anal. Chem.* 63:1282–1288.

Bard, A. J., F.-R. F. Fan, and M. V. Mirkin. 1994. Scanning electrochemical microscopy. *In* Electroanalytical Chemistry, Vol. 18. A. J. Bard, editor. Marcel Dekker, New York. 243–373.

Bard, A. J., F.-R. F. Fan, D. T. Pierce, P. R. Unwin, D. O. Wipf, and F. Zhou. 1991b. Chemical imaging of surfaces with the scanning electrochemical microscope. *Science.* 254:68–74.

Barker, A. L., M. Gonsalves, J. V. Macpherson, C. J. Slevin, and P. R. Unwin. 1999. Scanning electrochemical microscopy: beyond the solid/liquid interface. *Anal. Chim. Acta.* 385:223–240.

Barker, A. L., J. V. Macpherson, C. J. Slevin, and P. R. Unwin. 1998. Scanning electrochemical microscopy (SECM) as a probe of transfer processes in two-phase systems: theory and experimental applications of SECM-induced transfer with arbitrary partition coefficients, diffusion coefficients and interfacial kinetics. *J. Phys. Chem. B.* 102:1586–1598.

Bath, B. D., R. D. Lee, H. S. White, and E. R. Scott. 1998. Imaging molecular transport in porous membranes. Observation and analysis of electroosmotic flow in individual pores using the scanning electrochemical microscope. *Anal. Chem.* 70:1047–1058.

Bernich, E., R. Rubenstein, and J. S. Bellin. 1976. Membrane transport properties of bovine articular cartilage. *Biochim. Biophys. Acta.* 448: 551–561.

Bicher, H. I., and D. F. Bruley, editors. 1973. Oxygen Transport to Tissue. Instrumentation, Methods and Physiology. Plenum Press, London.

Burstein, D., M. L. Gray, A. L. Hartman, R. Gipe, and B. D. Foy. 1993. Diffusion of small solutes in cartilage as measured by nuclear magnetic resonance spectroscopy and imaging. *J. Orthop. Res.* 11:465–478.

Carleton, H. M. 1980. Carleton's Histological Technique. Oxford University Press, Oxford.

Fischer, A. E., T. A. Carpenter, J. A. Tyler, and L. D. Hall. 1995. Visualisation of mass transport of small organic molecules and metal ions through articular cartilage by magnetic resonance imaging. *Magn. Reson. Imaging.* 13:819–826.

Fournier, R. 1999. Basic Transport Phenomena in Biomedical Engineering. Taylor and Francis, Philadelphia.

Gribbon, P. M., A. Maroudas, K. H. Parker, and C. P. Winlove. 1998. Water and solute transport in the extracellular matrix: physical principles and macromolecular determinants. *In* Connective Tissue Biology. Integration and Reductionism. R. K. Reed and K. Rubin, editors. Portland Press, London. 95–123.

Hansma, P. K., B. Drake, O. Marti, S. A. C. Gould, and C. B. Prater. 1989. The scanning ion-conductance microscope. *Science.* 243:641–643.

Horky, D. 1993. The submicroscopic structure of articular cartilage in the adult pig. *Acta Vet. Brno.* 62:9–18.

Hunziker, E. B., M. Michel, and D. Studer. 1997. Ultrastructure of adult human articular cartilage matrix after cryotechnical processing. *Microscopy Research and Technique.* 37:271–284.

Jurvelin, J. S., D. J. Müller, M. Wong, D. Studer, A. Engel, and E. B. Hunziker. 1996. Surface and subsurface morphology of bovine humeral articular cartilage as assessed by atomic force and transmission electron microscopy. *J. Struct. Biol.* 117:45–54.

Keuttner, K. E., R. Schleyerbach, J. G. Peyron, and V. C. Hascall, editors. 1992. Articular Cartilage and Osteoarthritis. Raven Press, New York.

Knauss, R., G. Fleischer, W. Grunder, J. Kärger, and A. Werner. 1996. Pulsed field gradient NMR and nuclear magnetic relaxation studies of water mobility in hydrated collagen II. *Magn. Reson. Med.* 36:241–248.

Korchev, Y. E., C. L. Bashford, M. Milovanovic, I. Vodyanoy, and M. J. Lab. 1997. Scanning ion conductance microscopy of living cells. *Biophys. J.* 73:653–658.

Kwak, J., and A. J. Bard. 1989. Scanning electrochemical microscopy. Theory of the feedback mode. *Anal. Chem.* 61:1221–1227.

Macpherson, J. V., M. A. Beeston, P. R. Unwin, N. P. Hughes, and D. Littlewood. 1995a. Scanning electrochemical microscopy as a probe of local fluid flow through porous solids. *J. Chem. Soc. Faraday Trans.* 91:1407–1410.

Macpherson, J. V., M. A. Beeston, P. R. Unwin, N. P. Hughes, and D. Littlewood. 1995b. Imaging the action of fluid flow blocking agents on dentinal surfaces using a scanning electrochemical microscope. *Langmuir.* 11:3959–3963.

Macpherson, J. V., D. O'Hare, P. R. Unwin, and C. P. Winlove. 1997. Quantitative spatially resolved measurements of mass transfer through laryngeal cartilage. *Biophys. J.* 73:2771–2781.

Maroudas, A. 1970. Distribution and diffusion of solutes in articular cartilage. *Biophys. J.* 10:365–379.

Maroudas, A. 1975. Biophysical chemistry of cartilaginous tissue with special reference to solute and fluid transport. *Biorheology.* 12:233–248.

Matsue, T., H. Shiku, H. Yamada, and I. Uchida. 1994. Permselectivity of voltage-gated alamethicin ion channel studied by microamperometry. *J. Phys. Chem.* 98:11001–11003.

Mirkin, M. V., F.-R. F. Fan, and A. J. Bard. 1992. Scanning electrochemical microscopy, part 13. Evaluation of the tip shapes of nanometer size microelectrodes. *J. Electroanal. Chem.* 328:47–62.

Mow, V. C., M. H. Holmes, and W. M. Lai. 1984. Fluid transport and mechanical properties of articular cartilage: a review. *J. Biomech.* 17: 377–394.

Muehleman, C., and C. H. Arsenis. 1995. Articular cartilage, part II: the osteoarthritic joint. *J. Am. Podiatr. Med. Assoc.* 85:282–286.

Potter, K., R. G. S. Spencer, and E. W. McFarland. 1997. Magnetic resonance microscopy studies of cation diffusion in cartilage. *Biochim. Biophys. Acta.* 1334:129–139.

Roberts, S., J. P. G. Urban, H. Evans, and S. M. Eisenstein. 1996. Transport properties of the human cartilage endplate in relation to its composition and calcification. *Spine.* 21:415–420.

Saito, Y. 1968. Theoretical study on the diffusion current at the stationary electrodes of circular and narrow band types. *Rev. Polarogr.* 15: 177–187.

Scott, E. R., A. I. Laplaza, H. S. White, and J. B. Phipps. 1993a. Transport of ionic species in skin—contribution of pores to the overall skin conductance. *Pharm. Res.* 10:1699–1709.

Scott, E. R., J. B. Phipps, and H. S. White. 1995. Direct imaging of molecular transport through skin. *J. Invest. Dermatol.* 104:142–145.

Scott, E. R., H. S. White, and J. B. Phipps. 1991. Scanning electrochemical microscopy of a porous membrane. *J. Membr. Sci.* 58:71–87.

Scott, E. R., H. S. White, and J. B. Phipps. 1993b. Ionophoretic transport through porous membranes using scanning electrochemical microscopy—application to in vitro studies of ion fluxes through skin. *Anal. Chem.* 65:1537–1545.

Shrive, N. G., and C. B. Frank. 1994. Articular cartilage. *In* Biomechanics of the Musculo-Skeletal System. B. Nigg and W. Herzog, editors. J. Wiley and Sons, Chichester. 79–105.

Stockwell, R. A. 1983. Metabolism of cartilage. *In* Cartilage, Vol. 1. Structure, Function and Biochemistry. B. K. Hall, editor. Academic Press, London. 253–280.

Torzilli, P. A., J. M. Arduino, J. D. Gregory, and M. Bansal. 1997. Effect of proteoglycan removal on solute mobility in articular cartilage. *J. Biomech.* 30:895–902.

Torzilli, P. A., D. A. Grande, and J. M. Arduino. 1998. Diffusive properties of immature articular cartilage. *J. Biomed. Mater. Res.* 40:132–138.

Unwin, P. R., J. V. Macpherson, M. A. Beeston, N. J. Evans, N. P. Hughes, and D. L. Littlewood. 1997. New electrochemical techniques for probing phase transfer dynamics at dental interfaces in vitro. *Adv. Dent. Res.* 11:548–559.

Urban, J., and A. Hall. 1992. Physical modifiers of cartilage metabolism. *In* Articular Cartilage and Osteoarthritis. K. E. Keuttner, R. Schleyerbach, J. G. Peyron, and V. C. Hascall, editors. Raven Press, New York. 393–406.

Weinberg, P. D., S. L. Carney, C. P. Winlove, and K. H. Parker. 1997. The contributions of glycosaminoglycans, collagen and other interstitial components to the hydraulic resistivity of porcine aortic wall. *Connect. Tissue Res.* 36:297–308.